# Real-Time Force-Feedback Micromanipulation Using Mobile Microrobots With Colored Fiducials

Maria Guix, Jianxiong Wang, Ze An, Georges Adam, and David J. Cappelleri

*Abstract*—**This letter reports the design and fabrication of wirelessly controlled mobile microrobots with an on-board vision-based two-dimensional microforce sensor for use in force-guided micromanipulation tasks. The microforce sensing mobile microrobots ($\mu$FSMM) presented here exhibit compliant end-effectors with different stiffnesses and color tracking fiducials, which are used in conjunction with computer vision algorithms to provide real-time microforce feedback to the user when performing teleoperated micromanipulation tasks. The stiffness of the compliant springs has been tailored to provide an *in situ* micronewton level force detection capability with sub-$\mu$N resolution for the first time to mobile microrobots. The $\mu$FSMMs can be used in the fields of mechanobiology, theranostics, and for force-guided micromanipulation tasks with delicate structures, such as biological cells.**

*Index Terms*—**Micro/nano robots, visual tracking, biological cell manipulation.**

## I. Introduction

ROBOTS at the nano- and microscale have numerous applications in medicine and biology as well as applications in advanced manufacturing [1]. The major challenges with robots this small is in their design, fabrication, actuation, and wireless control. A popular approach to actuating microrobots for medical applications is using external magnetic fields [2]. This non-invasive external energy source allows for different motion control methods [3]–[5] and also the possibility of closed-loop path-planning and control [6] when coupled with a visual tracking system for the robot.

It is desired to provide microrobots with enhanced capabilities and functions other than just locomotion in order for them to realize their full potential [7]. The accurate characterization of mechanical properties in biological materials (i.e., tissue, cells) is crucial to understanding the related biological events taking place. Mechanobiology [8] studies revealed the importance of the mechanotransduction processes [9], pointing out the need for safe biomanipulation, especially when it comes to single cell manipulation tasks so that cells do not get damaged during the course of manipulation. In this context, real-time micromanipulation force sensing during these studies is critical.

Finely controlled microrobots are applicable to both single-cell manipulation [10], [11] and the arrangement of cells in particular configurations (scaffolds) for tissue engineering applications [12]. The integration of micro-force sensing capabilities to mobile microrobots is desired for expanding their possible applications for intelligent biomanipulation and micromanipulation tasks, fundamental mechanobiological studies, and medical applications for advanced theranostics [7], [13], [14], [15].

Micro-force sensing in general has been implemented into MEMS devices mounted to stationary micromanipulators sensing forces in a variety of ways [16]–[19]. Only limited work has been done in the area of mobile microrobotics with force-sensing. In [20], the authors demonstrate an on-chip microrobot with a silicon beam structured force sensing end-effector. This is actually a millimeter scale microrobot can only detect one-dimensional mN level forces in an off-line manner. There is a robotic system with nano-Newton level force sensing capabilities presented in [21]. These robots are also mm-scale robots and use modified AFM cantilevers to sense the force in one dimension.

In our previous, we presented the micro-force sensing mobile microrobot ($\mu$FSMM) that can perform on-board vision-based micro-force sensing in two-dimensions by optically determining the deformation of a calibrated elastic structure that deforms when manipulating an object of interest [22], [23]. The vision-based sensor relies on a compliant polydimethylsiloxane (PDMS) spring end-effector, that is able to exert forces at the $\mu$N level. A magnetic body on the robot allows for it to be controlled with external magnetic fields. While micro-scale $\mu$FSMM prototypes were obtained and proof of concept micromanipulation tasks performed, the vision-based force sensing was not able to be performed in real-time. In this letter, we present a new generation of $\mu$FSMM designs that include different end-effectors designs for micromanipulation, distinct geometrical features on the outer edge of the frame of the robot along with the novel integration of colored structures in the $\mu$FSMM body as distinctive fiducials to facilitate real-time optical recognition algorithms (Fig. 1). The PDMS composition of the springs has been customized and color-coded to achieve lower stiffness values and extend the sensing range further down the $\mu$N scale achieving sub-$\mu$N force sensing resolution for the first time. Two real-time image processing algorithms have been implemented and com-

Manuscript received February 24, 2018; accepted June 26, 2018. Date of publication July 11, 2018; date of current version August 2, 2018. This letter was recommended for publication by Associate Editor S. Régnier and Editor Y. Sun upon evaluation of the reviewers' comments. This work was supported by National Science Foundation under Grants IIS 1149827, NRI 1637961, NSF IIS 1358446 and NSF IIS 1433967. *(Corresponding author: David J. Cappelleri.)*

The authors are with the Multi-Scale Robotics and Automation Lab, School of Mechanical Engineering, Purdue University, West Lafayette, IN 47906 USA (e-mail: mguixnog@purdue.edu; wang1822@purdue.edu; an40@purdue.edu; adamg@purdue.edu; dcappell@purdue.edu).

This letter has supplementary downloadable material available at http://ieeexplore.ieee.org, provided by the authors. The Supplementary Materials contain videos showing the experimental results for the uFSMM associated with Fig. 7 and 8 in the paper. This material is 14.4 MB in size.

Digital Object Identifier 10.1109/LRA.2018.2854909

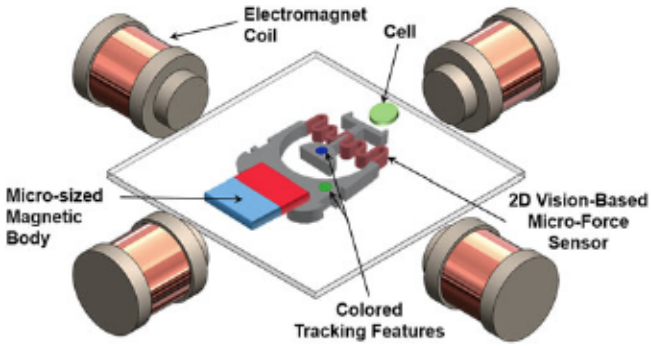


Fig. 1. Main components of the micro-force sensing mobile microrobot ($\mu$FSMM). The robot moves from magnetic field gradients generated by an electromagnetic coil system. The vision-based force sensor relies on the optical detection of deformation of a calibrated compliant spring structure when a force is applied to the end-effector. Colored tracking features are implemented for robust tracking and real-time force-sensing.

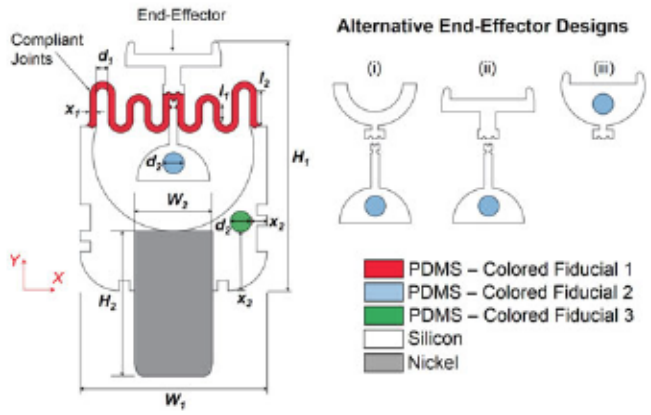


Fig. 2. Schematic of the $\mu$FSMM. The microrobot consists of a rigid silicon frame, colored compliant PDMS joints, rigid silicon end-effectors, colored PDMS tracking fiducials, and a nickel magnetic body. Key dimensions for the design are the following (units = $\mu$m): $W_1 = 719$ to 735, $H_1 = 1144$ to 1283, $W_2 = 300$, $H_2 = 555$, $x_1 = 25$, $d_1 = 45$, $l_1 = 50$, $l_2 = 122$, $d_2 = 80$, $x_2 = 60$, and $x_3 = 225$. The thickness of the microrobot and compliant structure is 80 $\mu$m.

pared to provide real-time force feedback information to a user teleoperating the $\mu$FSMMs in the workspace. Experimental tests demonstrate that the real-time force-feedback provided to the end user permits the safe micromanipulation of micro-objects by making sure the applied forces remain around a desired threshold so that cells are not damaged by excessive manipulation forces.

## II. Microrobot Design & Fabrication

A schematic for the $\mu$FSMM design is shown in Fig. 2. The micro-scale robot consists of three main parts: (i) a compliant structure attached to a rigid end effector, (ii) colored features embedded in a rigid body that is attached to a (iii) magnetic body. Three different types of rigid end-effector designs have been explored for manipulating different types and shapes of micro-objects. The polymeric spring structures serve as a 2D vision-based micro-force sensor. (We refer the reader to [7] for a summary of the modeling and geometry optimization performed on these structures). The foot-print of the $\mu$FSMMs range from 719 to 735 $\mu$m $\times$ 1144 to 1283 $\mu$m for the different designs explored. In our previous work [7], [22], [23], the tracking of the displacements of the probe tip with respect to the robot used to sense the 2D micro-forces was not able to be done in real-time. This was due to the fact that the intricacies of the vision-algorithms were not considered during the design of the actual microrobot. With this knowledge in mind, sharp corners and cut-out features are added to the edges of the silicon frame in the designs, as well as novel colored tracking fiducials incorporated into the robot body, as shown in Fig. 2. These new features allow for the implementation of two different real-time tracking techniques. Both provide real-time micro-force feedback information to the user teleoperating the robots to accomplish micromanipulation tasks.

Both the spring and colored features consist of polydimethylsiloxane (PDMS, Sylgard 184 silicone elastomer kit), a polymer typically used in prototyping and lab-on-a-chip devices. In our particular case, we added a silicone pigment to the usual base and agent mixture in order to tune its color, as described in [24]. Blue, red, and green colors were chosen in order to facilitate RGB value identification in the vision-based tracking method. Additionally, two base/curing agent ratios were used with dyes to obtain color-coded elastomeric springs with different stiffness values: (i) 10:1 being the standard recommended ratio for red-dyed spring structures, and (ii) 16.7:1 for the blue-dyed structures with lower network cross-linking, as reported in [25]. Lower stiffness permits the spring deformation under lower applied forces, allowing for the detection of forces in the low $\mu$N range.

A new fabrication process was designed in order to implement the different colored PDMS features into the microrobot, as shown in Fig. 3. It is based on a multi-step photolithography method where positive deep reactive etching (DRIE) is used to obtain both the mold where the PDMS spring structure will be later cured and the microrobot rigid components [26]. AZ1518 positive photoresist is first spin-coated at 1000 rpm for 30 seconds and then soft baked for 3 minutes at 100 °C. The full wafer is then exposed for 30 seconds in a mask aligner (UV (350–400 nm), Suss MA 6 Mask Aligner, SUSS MicroTec) using a mask with the spring design. The removal of the non-polymerized photoresist is done by using MF CD-26 developer (Microchem Inc., USA) for 30 seconds. After a post exposure bake of 3 minutes at 100 °C (step 1, Fig. 3), the DRIE process (step 2) is used to create the trench with the final desired thickness of $\mu$FSMM itself. PDMS is mixed at a base/curing agent ratio of 10:1 or 16.7:1 and the corresponding pigment, and degassed for 30 minutes. The colored PDMS is spin coated at 2000 rpm for 30 seconds. The excess PDMS is removed using a silicone spatula and cured at room temperature for 24 hours (step 3). The wafer surface is then cleaned with acetone (step 4). The creation of both colored fiducials consists of the same steps described above, except for the PDMS curing time is now 20 minutes at 120 °C. The corresponding steps are depicted in Fig. 3 in the steps 5–8 and 9–12 for the green and red colored fiducials, respectively. It should be noted that after depositing and curing the green PDMS (step 7), a cleaning process with acetone is done (step 8) before applying AZ1518 to define the red fiducial (step 9). The $\mu$FSMM solid body is

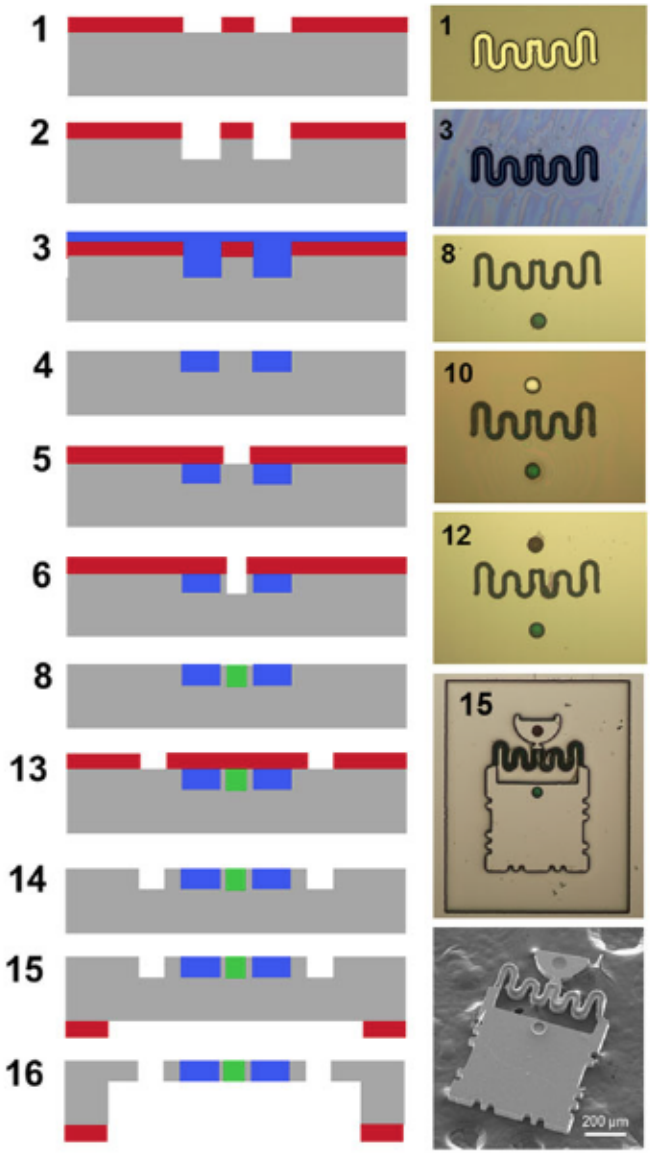


Fig. 3. Fabrication process of $\mu$FSMM based on a multi-step photolithography method. A trench for the spring structure created first. Colored (blue or red) PDMS is then applied and cured. The same steps are followed in order to create the colored red and green tracking fiducials. The $\mu$FSMM solid body is obtained by etching the silicon wafer around the colored PDMS structures. After a backside etching around the $\mu$FSMM structure is freed and then a Ni magnetic body is assembled to the silicon frame.

then defined by photo patterning AZ1518 with the $\mu$FSMM body mask (step 13) and a DRIE process. After another acetone cleaning step, the final $\mu$FSMM is ready to be released (step 15). A back-side window is photo-patterned using the AZ9260 photoresist (step 16). The $\mu$FSMM are individually collected after the backside etching process (step 17). A nickel (Ni) magnetic body is manufactured separately by a chemical etching process (www.fotofab.com) and then manually assembled to the silicon frame using tweezers and glue.

The $\mu$FSMMs are actuated and guided under magnetic field gradients generated by homemade Helmholtz coils (two pairs of electromagnetic coils arranged symmetrically along a common axis). The microrobots are placed inside a petri dish located

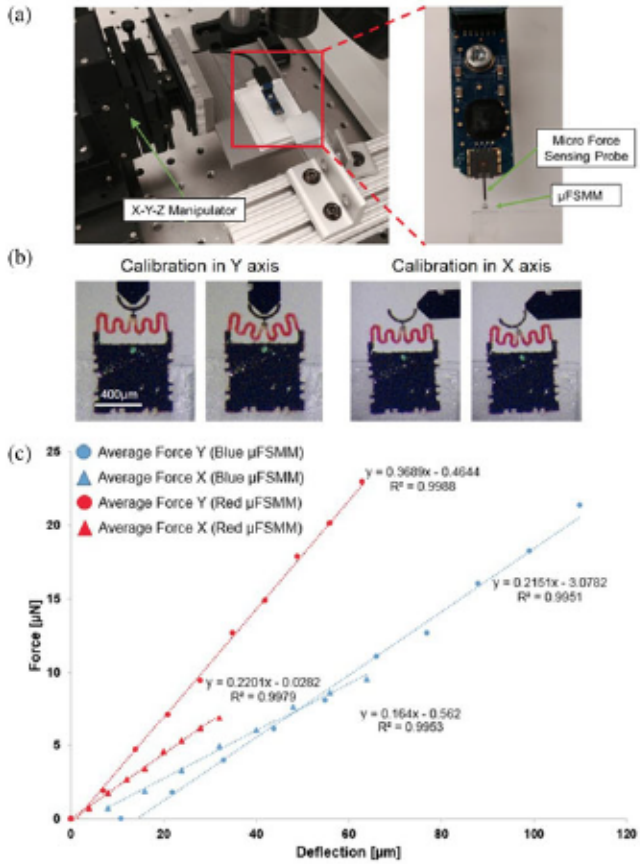


Fig. 4. $\mu$FSMM end-effector stiffness calibration: (a) Calibration setup with 3 degree of freedom manipulator and micro-force sensing probe. (b) $T_i$: initial position (undeflected); $T_f$: final position (maximum deflection). (c) Calibration data plot for x and y axis tests for two different $\mu$FSMMs. The stiffness is significantly different between the color-coded $\mu$FSMMs with different PDMS component mixing ratios.

in the workspace between the four coils, where field gradients greater than 0.5 T/m can be applied. An overhead camera is used for tracking the microrobot pose and deformations for force-sensing.

## III. Real-Time Vision-Based Micro-Force Sensing

There are two key components required for real-time vision-based micro-force sensing. The first is an accurate calibration of the stiffness of the PDMS springs in both the X and Y directions. The second is the actual image-processing algorithm used to determine the real-time displacement of the calibrated structures. Each of these critical components are described in the following sections.

### A. $\mu$FSMM Calibration

The compliant end-effectors need to be calibrated in order to determine their stiffness in the x and y direction ($K_x$ and $K_y$, respectively) The calibrations are conducted using a micro-force sensor probe (FT-S1000, FemtoTools) mounted on a micromanipulator arm (MP-225, Sutter Instrument) that can translate in XYZ directions independently (Fig. 4(a) and (b)). The forces measured by the probe are recorded for different end-effector

TABLE I
$\mu$FSMM CALIBRATION RESULTS

| Robot # | Spring Color | Stiffness (N/m) | | Sensing Range ($\mu$N) | | Resolution ($\mu$N) | |
|---|---|---|---|---|---|---|---|
| | | $K_x$ | $K_y$ | X | Y | X | Y |
| 1 | Light Red | 0.220 | 0.369 | [0, 11] | [0, 60] | 1.36 | 2.28 |
| 2 | Light Red | 0.652 | 0.526 | [0, 61] | [0, 110] | 4.02 | 3.24 |
| 3 | Dark Red | 0.059 | 0.047 | [0, 4] | [0, 10] | 0.36 | 0.29 |
| 4 | Dark Red | 0.062 | 0.186 | [0, 8] | [0, 31] | 0.38 | 1.15 |
| 5 | Dark Red | 0.131 | 0.196 | [0, 16] | [0, 44] | 0.81 | 1.21 |
| 6 | Light Blue | 0.164 | 0.215 | [0, 13] | [0, 25] | 1.01 | 1.33 |
| 7 | Dark Blue | 0.087 | 0.171 | [0, 13] | [0, 26] | 0.53 | 1.05 |

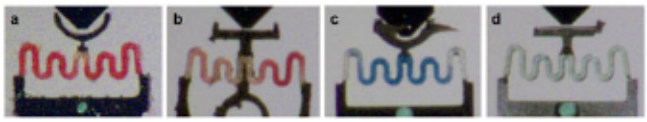


Fig. 5. Color-coded springs: PDMS mixing ratio 10:1 = red, 17.6:1 = blue. (a) dark red, (b) light red, (c) dark blue, (d) light blue.

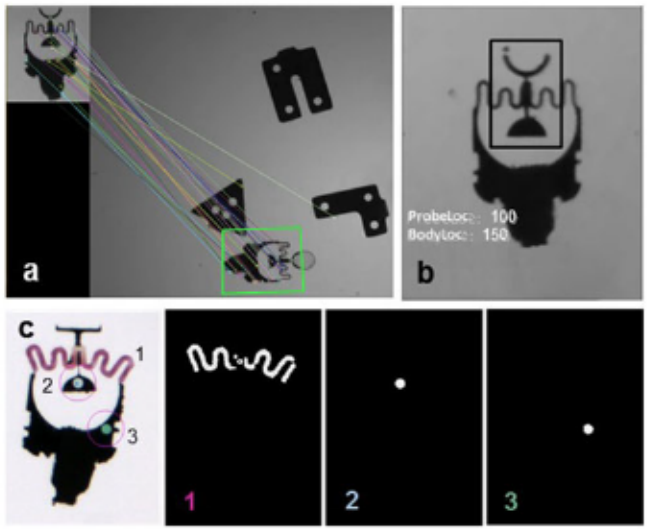


Fig. 6. (a) SURF detection of the microrobot; (b) Template matching tracking result and associated image locations of robot probe and body; (c) Color-tracking method: raw image frame and color matching results associated to the segmented (1) spring, (2) robot probe fiducial, and (3) body fiducial.

deflections, set by the displacement of the micromanipulator. This information is plotted, as shown in Fig. 4(c), and the stiffness in the x and y directions is calculated by analyzing the slope of a linear trendline going through the data points. During the fabrication procedure, $\mu$FSMMs with different PDMS mixing ratios were produced and color-coded (red for 10:1 ratio and blue for 17.6:1 ratio), to obtain different stiffness and thus, different force sensing ranges for designs with the same geometry. As expected, the stiffness of a red spring robot is greater than the blue one (Fig. 4(c)). In this case, the stiffness of a red robot (Robot 1 from Table I) is $K_x = 0.220$ N/m, $K_y = 0.369$ N/m, and the stiffness of a blue robot (Robot 7) is $K_x = 0.087$ N/m, $K_y = 0.171$ N/m. Interestingly, another factor that affects the stiffness of the end-effector is the amount of colored dye used in the compliant structure (Fig. 5). The more dye present, the more vibrant the color, and interestingly lower the stiffness. This was observed during the fabrication process when the PDMS becomes less viscous with the mixture of dye, signifying a smaller stiffness. This was also verified during the device calibration tests as shown in Table I. The sensing range reported is the maximum force that can be measured by the vision-based sensor before the deflected spring contacts the silicon frame. The reported force sensing resolution is the minimum force measurable based on the camera resolution of 6.17 $\mu$m/pixel and a displacement tracking accuracy of 1 pixel. The table shows that we can tailor the stiffness values of the $\mu$FSMMs to range from 0 $\mu$N to 110 $\mu$N along with obtaining sub-$\mu$N force sensing resolutions along each axis. For reference, the $\mu$FSMMs in our previous generations only had force sensing ranges between 0 $\mu$N and 20 $\mu$N and resolutions on the order of $\mu$Ns.

To investigate if the calibrated stiffness of the robots change over time, two robots were calibrated multiple times over 8 days. The standard deviation of the measured stiffness values was calculated and compared to the average stiffness in each direction. The average standard deviation in the stiffness values correspond to at most a change in detected force of only 0.08 $\mu$N for 1 pixel displacement (6.17 $\mu$m). Therefore, small daily variations in the $\mu$FSMM stiffness values will not have a significant effect on the measured force values.

### B. Real-Time Image Processing

To sense the micro-forces being applied by the $\mu$FSMMs, the relative displacement between the rigid body of the microrobot and the moving tip (probe) of the end-effector needs to be determined using computer vision techniques. Each tracking method developed is first initialized by loading the calibration data specific to the $\mu$FSMM robot being used. For the vision system used, the pixel to $\mu$m ratio is approximately 6 $\mu$m/pixel and the camera runs at 40 Hz. The system consists of a 1.3 MP CMOS camera (PointGrey e2v EV76C560) with an adjustable lens system with magnification ranging from 0.75x to 4.5x. The illumination is done using a LED ring placed underneath the workspace. The developed algorithms are run on a desktop computer with an Intel Core i7-6950x CPU running at 3.00 GHz, 48 GB of RAM.

*1) SURF-Based Tracking:* The SURF (Speeded-up Robust Feature) algorithm [27] is used to identify feature points on a template of the robot and in the associated live camera image. The algorithm utilizes the newly added sharp features on the edges of the silicon frame of the robot. Next, a 2D homography is used to track the position and orientation of the robot in each camera frame, as shown in Fig. 6(a). With this information, an affine transformation is then applied to obtain a rectified region of interest (ROI) image of the robot. The sum-of-squared-difference (SSD) template matching algorithm is used next to locate the centroids of the end-effector tip (probe) and the body of the robot using manually selected templates for each during initialization at the beginning of the program. The deformation of the compliant structure is then calculated based on the difference between the coordinates of the center of the probe and the centroid of the robot body in the deformed image and that same distance in an image of the microrobot in its undeformed state. In Fig. 6(b), numbers associated with the *ProbeLoc* and *BodyLoc* labels are the locations of the probe center and the body center

in pixel units, respectively. The conversion from displacement to force is calculated through the observed deformation and the stiffness values obtained from the calibration data. This algorithm only runs at 5 Hz when utilizing the hard-drive of the desktop computer. Therefore, an NVIDIA GeForce GTX 1080 graphics card was installed and the OpenCV GPU module with the CUDA speed up feature was implemented to speed up performance. With this, the algorithm is able to run in real-time at 12 Hz along with the magnetic control system. While this technique provides for real-time force feedback, faster speeds are desired. Additionally, when the robot moves fast, the features that are being tracked can be blurred and tend to become unstable which leads to skipped frames and lost feedback data to the user. Therefore, a more robust, stable, and faster approach is needed.

*2) Color-Based Tracking:* While the SURF-based algorithm runs at real-time, it involves intensive computations (that require GPU processing) that limits the real-time speed of the vision-based force measurement that can be achieved. This feature detection method can also induce uncertainty due to the use of the 2D homography process. As previously mentioned, when the robot undergoes sudden rotational motion, its features are blurred due to the limited frame rate and the tracking breaks down. Therefore, we have developed a color-based tracking technique that is more stable and less computationally expensive.

The color-based tracking algorithm is first initialized by tuning the HSV (hue, saturation, and value) parameters for the red, blue, and green colors that are to be detected on the robot (Fig. 6(c)). After this, for each image frame, image dilation and erosion preprocessing algorithms are applied, the image is converted from RGB to HSV values, and color-thresholding is applied to determine the robot position and orientation in the workspace. The robot pose is determined using the color-tracked features. Principal component analysis (PCA) is used to determine the centroid of and orientation of the segmented spring structure in the image (Fig. 6(c)(1)) and thus the robot pose. At startup, the robot is set up so it is not in contact with any other objects in the workspace and is in its undeformed state. The initial pose of the robot is determined by searching the entire image in the first five image frames. Once the program detects the robot's pose in the first five frames, the search space is reduced in subsequent images frames from the original image to just a region of interest (ROI) approximately two times of the size of the robot around the position of the robot in the previous frame. This is done since the robot will not displace an amount larger than the ROI in two consecutive frames. These first five image frames are also use to record the undeformed distances between the centroids of each of the color-tracked objects on the robot. To track the displacement of the spring, similar templates and the sum square difference (SSD) tracking can be used, as done in the case of the SURF-based tracking technique. In this case, the deformed and undeformed distance between the centroid of the spring (probe, (Fig. 6(c)(1))) and the centroid of the body template are used to calculate the deformation. This works well but it can suffer from similar stability issues when the robot undergoes sudden rotations. However, using the change in magnitude of a vector between the centroids of the circular color-tracked fiducials ((Fig. 6(c)(2) and (3)) to calculate the deformation provides more stable and consistent force information than the template tracking method. For both displacement measures, each are projected to the robot's x and y-axes to determine the respective x and y displacements for use in the stiffness calibration curves to provide real-time 2D micro-force feedback to the user. This color-based tracking technique operates at 20 Hz without the aid of GPU programming. This is an improvement of 67% over the SURF-based tracking technique with GPU programming and 4X faster than without GPU programming.

TABLE II
MICRO-FORCE SENSING ACCURACY

| Frame Number | Y-Force Value ($\mu$N) | | Percentage Error (%) |
|---|---|---|---|
| | Manual | Vision | |
| 184 | 4.32 | 4 | 7.55 |
| 185 | 15.34 | 17 | 10.79 |
| 186 | 19.49 | 19 | 2.52 |
| 187 | 22.35 | 24 | 7.39 |
| 188 | 23.47 | 24 | 2.26 |
| 190 | 20.50 | 22 | 8.72 |
| 191 | 20.07 | 24 | 8.72 |
| 192 | 21.87 | 24 | 9.71 |
| 193 | 27.26 | 27 | 0.97 |
| 194 | 26.71 | 27 | 1.08 |

The performance accuracy of the color-based tracking algorithm was assessed through comparisons with off-line force measurements as ground truth, where a user manually selecting feature points in each image frame for displacement calculations. This was done for the Y-direction forces values for three test pushes consisting of sets of 10 image frames each. Table II shows this data for one of the test pushes that was evaluated. Note: while the vision system is capable of sub-$\mu$N level resolution, the values for the detected forces were rounded to the nearest integer value here to investigate the extreme case. Across the 30 image frames for all three pushes, the average percentage error for the color-based tracking system is approximately 6% of the ground truth value. This corresponds to an average accuracy of less than $\pm 1$ $\mu$N.

## IV. EXPERIMENTAL RESULTS

A set of manipulation experiments were performed with the new $\mu$FSMMs designs and color-based real-time tracking algorithms that were developed. In the first set of experiments, a user was instructed to perform a micromanipulation test by teleoperating a $\mu$FSMM with and without force-guiding. Force-guiding is defined here as the displaying of the real-time micro-force feedback information to screen. When the force value exceeds a predefined force threshold, the display text showing the real-time force-feedback values turns from green to red to warn the user that they have exceeded this value. For each test, the user was instructed to remotely control the $\mu$FSMM (Robot 2 from Table I) to first apply three control pushes to a fixed object in the scene to get used to how the $\mu$FSMM operates and then to use the

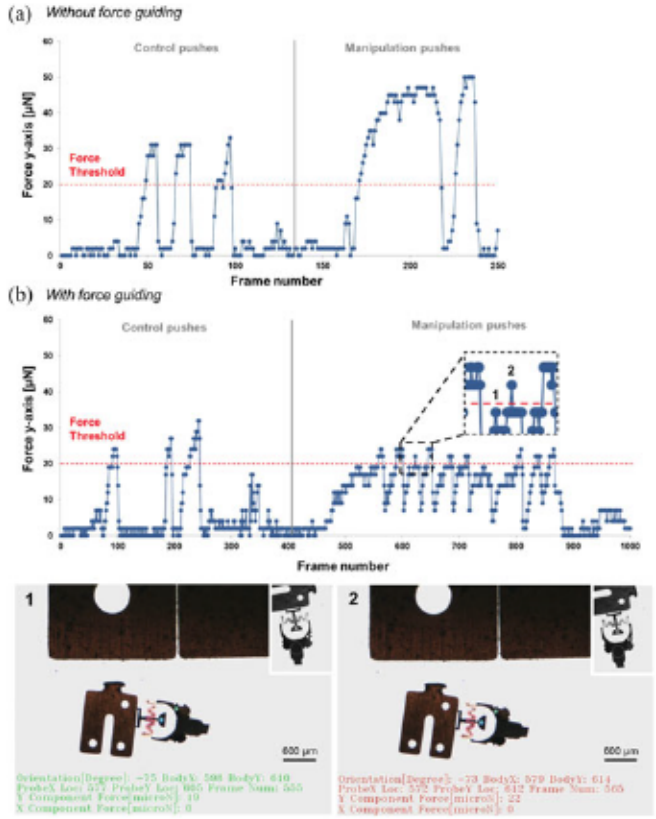


Fig. 7. Force-guided transport experiment with Robot 2 from Table I. (a) Real-time force applied to the micro-part without force-guided feedback to the user vs image frame. The max manipulation forces is approximately 50 $\mu$N. (b) Real-time force applied to the micro-part with force-guided feedback to the user vs image frame. The max manipulation force threshold feedback to the user is 20 $\mu$N; The max manipulation force applied is approximately 25 $\mu$N. Images 1 and 2 show the force-guided feedback to the user during the experiment from before and after the designated maximum force threshold is exceeded.

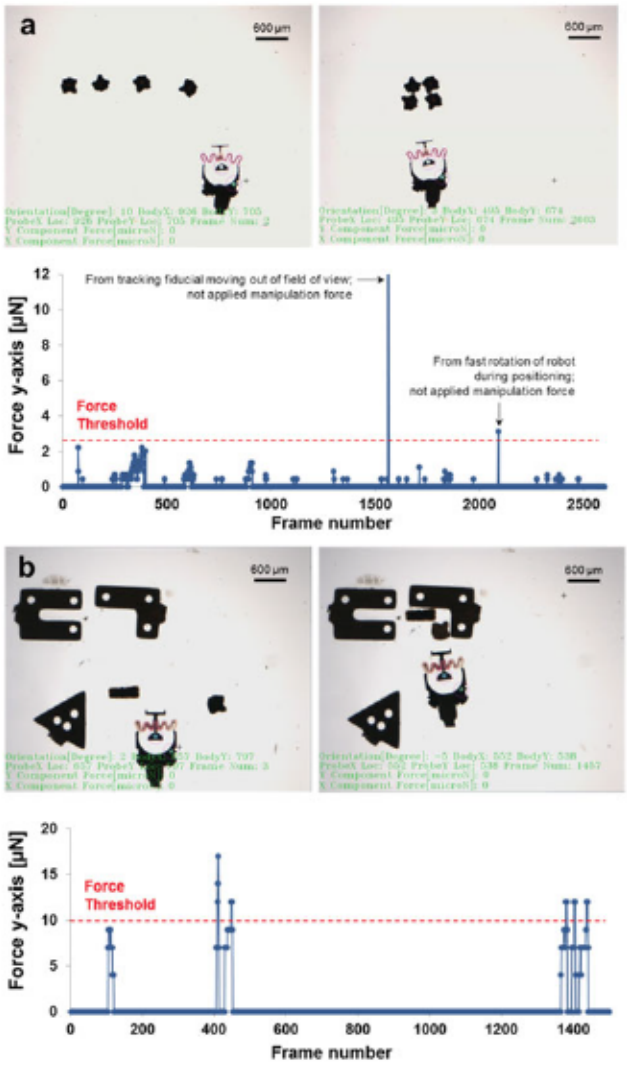


Fig. 8. Force-guided micromanipulation and microassembly experiments. (a) Screen shots and force plot from Robot 3 safely arranging polygonal micro-objects from a straight line configuration to a square shape with a force threshold of 3 $\mu$N. (b) Screen shots and force plot for Robot 2 assembling micro-parts towards fixed obstacles in the workspace with a prescribed force threshold of 10 $\mu$N.

$\mu$FSMM to translate a micro-part across the workspace. Fig. 7 shows the results from a micromanipulation test without and with force-guiding. Fig. 7(a) is the case without force-guiding. Here, the control pushes resulted in forces of approximately 30 $\mu$N and the maximum manipulation forces when translating the micro-part were approximately 50 $\mu$N. Note: for these tests, the user is not shown any force information during the course of the experiment. For the force-guiding case Fig. 7(b), the control pushes resulted in maximum forces of around 30 $\mu$N again. However, now with the user utilizing the real-time force information on the screen and noting when the prescribed threshold has been met, the maximum manipulation forces applied are only about 25 $\mu$N. (Note: while the $\mu$FSMMs can sense forces in two dimensions, the x-direction forces in these experiments were negligible since the manipulations were along the robot's y-axis. Thus only the y-axis forces are reported.) These tests show that with real-time force-guiding, the user is able to limit the manipulation forces applied to the micro-object in the vicinity of a preset force threshold.

The next set of experiments, the user was tasked with a micromanipulation task to arrange a number of micro-objects into a prescribed pattern with force-guiding with a force threshold value of only 3 $\mu$N for the manipulation forces. Fig. 8(a) shows images and force plot information for one of these types of experiments using Robot 3. Here, the manipulated objects are polygonal SU8 micro-structures with a footprint of 150 $\mu$m $\times$ 150 $\mu$m and a thickness of 70 $\mu$m. The parts are manipulated from a straight line configuration into a square shape. None of the applied manipulation forces exceeded the force threshold. Note the low range and high resolution micro-force sensing provided by Robot 3, that was not previously possible.

Finally, in another set of force-guided experiments the user was instructed to manipulate micro-sized rectangular and square parts to assemble them with respect to fixed objects in the scene. The results of one of these experiments is shown in Fig. 8(b). With the use of force-guiding, the microassembly task is able to be accomplished without the allowable force threshold in the y-axis being exceeded. Live videos of each of the experiments described in this section are available in the supplemental material uploaded with this letter.

## V. CONCLUSION

In this letter, we have presented $\mu$FSMMs specifically designed for real-time vision-based micro-force sensing. A new fabrication process was designed to integrate colored tracking fiducials into the design. The color-based tracking algorithms are able to provide mobile microrobots with two-dimensional micro-force feedback in real-time at 20 Hz to the user for the first time. This force feedback information is used to guide the user to perform a host of teleoperated micromanipulation tasks in safe manner by displaying the real-time force feedback information on the screen and signaling the user when the manipulation force exceeds a pre-defined force threshold. The stiffness of the $\mu$FSMMs have been tuned by altering the PDMS base:curing agent ratios and adding in colored dyes to obtain lower stiffness and color-coded structures that provide a sub-$\mu$N level force sensing range, a higher resolution than was previously possible. The manipulation and sensing capabilities demonstrated by the $\mu$FSMM present them as a potential platform for safe biomanipulation and mechanobiology studies as well as the construction of 3D scaffolds in tissue engineering applications.

## ACKNOWLEDGMENT

The authors acknowledge the facility access at Purdue University's Birck Nanotechnology Center and the technical assistance from S. Rinehart and B. V. Johnson for graphic assessment.

## REFERENCES

[1] E. Diller and M. Sitti, "Micro-Scale mobile robotics," *Found. Trends Robot.*, vol. 2, no. 3, pp. 143–259, 2013.

[2] M. Sitti, *Mobile Microrobotics* (Intelligent Robotics and Autonomous Agents). Cambridge, MA, USA: MIT Press, 2017.

[3] W. Gao and J. Wang, "Synthetic micro/nanomotors in drug delivery," *Nanoscale*, vol. 6, no. 18, pp. 10486–10494, 2014. [Online]. Available: http://xlink.rsc.org/?DOI=C4NR03124E

[4] M. Sitti *et al.*, "Biomedical applications of untethered mobile milli/microrobots," *Proc. IEEE*, vol. 103, no. 2, pp. 205–224, Feb. 2015.

[5] X. Z. Chen *et al.*, "Recent developments in magnetically driven micro- and nanorobots," *Appl. Materials Today*, vol. 9, pp. 37–48, 2017. [Online]. Available: http://dx.doi.org/10.1016/j.apmt.2017.04.006

[6] T. Xu, J. Yu, X. Yan, H. Choi, and L. Zhang, "Magnetic actuation based motion control for microrobots: An overview," *Micromachines*, vol. 6, no. 9, pp. 1346–1364, Sep. 2015.

[7] W. Jing, S. Chowdhury, and D. Cappelleri, "Magnetic mobile microrobots for mechanobiology and automated biomanipulation," in *Microbiorobotics* (Micro and Nano Technologies), 2nd ed., M. Kim, A. A. Julius, and U. K. Cheang, Eds. Boston, MA, USA: Elsevier, 2017, ch. 10, pp. 197–219. [Online]. Available: https://www.sciencedirect.com/science/article/pii/B9780323429931000173

[8] P. Hersen and B. Ladoux, "Biophysics: Push it, pull it," *Nature*, vol. 470, no. 7334, pp. 340–341, Feb. 2011.

[9] D. E. Jaalouk and J. Lammerding, "Mechanotransduction gone awry," *Nature Rev., Mol. Cell Biol.*, vol. 10, pp. 63–73, Jan. 2009.

[10] Y. Shen and T. Fukuda, "State of the art: Micro-nanorobotic manipulation in single cell analysis," *Robot. Biomimetics*, vol. 1, no. 1, 2014, Art. no. 21.

[11] E. B. Steager *et al.*, "Automated biomanipulation of single cells using magnetic microrobots," *Int. J. Robot. Res.*, vol. 32, no. 3, pp. 346–359, Mar. 2013.

[12] S. Tasoglu, E. Diller, S. Guven, M. Sitti, and U. Demirci, "Untethered micro-robotic coding of three-dimensional material composition," *Nature Commun.*, vol. 5, Jan. 2014, Art. no. 3124.

[13] A. V. Singh and M. Sitti, "Targeted drug delivery and imaging using mobile milli/microrobots: A promising future towards theranostic pharmaceutical design," *Current Pharmaceutical Design*, vol. 22, no. 11, pp. 1418–1428, Mar. 2016.

[14] W. Shang, H. Lu, W. Wan, T. Fukuda, and Y. Shen, "Vision-based nano robotic system for high-throughput non-embedded cell cutting," *Sci. Rep.*, vol. 6, no. 1, Mar. 2016, Art. no. 22534.

[15] G. Lucarini, V. Iacovacci, P. J. Gouveia, L. Ricotti, and A. Menciassi, "Design of a novel magnetic platform for cell manipulation," *J. Micromechanics Microengineering*, vol. 28, no. 2, 2018, Art. no. 025009. [Online]. Available: http://stacks.iop.org/0960-1317/28/i=2/a=025009

[16] F. Beyeler, S. Muntwyler, and B. J. Nelson, "A six-axis MEMS force-torque sensor with micro-newton and nano-newtonmeter resolution," *J. Microelectromechanical Syst.*, vol. 18, no. 2, pp. 433–441, Apr. 2009.

[17] D. J. Cappelleri, G. Piazza, and V. Kumar, "A two dimensional vision-based force sensor for microrobotic applications," *Sensors Actuators A: Physical*, vol. 171, no. 2, pp. 340–351, 2011. [Online]. Available: http://www.sciencedirect.com/science/article/pii/S0924424711004043

[18] B. Komati, J. Agnus, C. Clevy, and P. Lutz, "Prototyping of a highly performant and integrated piezoresistive force sensor for microscale applications," *J. Micromechanics Microengineering*, vol. 24, no. 3, 2014, Art. no. 035018. [Online]. Available: http://stacks.iop.org/0960-1317/24/i=3/a=035018

[19] V. Guelpa, G. J. Laurent, P. Sandoz, and C. Clvy, "Vision-based microforce measurement with a large range-to-resolution ratio using a twin-scale pattern," *IEEE/ASME Trans. Mechatron.*, vol. 20, no. 6, pp. 3148–3156, Dec. 2015.

[20] T. Kawahara *et al.*, "On-chip microrobot for investigating the response of aquatic microorganisms to mechanical stimulation," *Lab on a chip*, vol. 13, pp. 1070–1078, 2013.

[21] J. Brufau *et al.*, "Micron: Small autonomous robot for cell manipulation applications," in *Proc. IEEE Int. Conf. Robot. Automat.*, Apr. 2005, pp. 844–849.

[22] W. Jing and D. J. Cappelleri, "Incorporating in-situ force sensing capabilities in a magnetic microrobot," in *Proc. IEEE/RSJ Int. Conf. Intell. Robots Syst.*, 2014, pp. 4704–4709.

[23] M. Guix, Z. An, J. Wang, B. Johnson, and D. Cappelleri, "Vision-based micro-force sensing mobile microrobots for intelligent micromanipulation," in *Proc. Int. Conf. Manipulation, Automat. Robot. at Small Scales*, Jul. 2017.

[24] F. Burgoyne, "Adding colour to PMDs chips for enhanced contrast," 2018. [Online]. Available: http://blogs.rsc.org/chipsandtips/2011/11/17/adding-colour-to-pmds-chip s-for-enhanced-contrast/. Accessed on: Feb. 23, 2018.

[25] Z. Wang, "Polydimethylsiloxane mechanical properties measured by macroscopic compression and nanoindentation techniques," Ph.D. dissertation, University of South Florida Tampa, FL, USA, 2011.

[26] A. P. Gerratt, I. Penskiy, and S. Bergbreiter, "Integrated silicon-PDMs process for microrobot mechanisms," in *Proc. IEEE Int. Conf. Robot. Automat.*, May 2010, pp. 3153–3158.

[27] H. Bay, T. Tuytelaars, and L. Van Gool, *SURF: Speeded Up Robust Features*. Berlin, Germany: Springer, 2006, pp. 404–417.